npj | Materials Degradation

www.nature.com/npjmatdeg

ARTICLE OPEN

Check for updates

Potentiodynamic polarization curves of AA7075 at high scan rates interpreted using the high field model

Hu Zhou[1,3], Danny Chhin[1,3], Alban Morel[2✉], Danick Gallant[2✉] and Janine Mauzeroll[1✉]

The drastic distortion of potentiodynamic polarization curves measured at high potential scan rates prevents the extraction of accurate kinetic parameters. In this work, we start by measuring potentiodynamic polarization curves of AA7075 at scan rates ranging from 0.167 mV·s^{-1} to 100 mV·s^{-1}, in an acidic 0.62 M NaH_2PO_4 solution and a near-neutral 3.5 wt% NaCl solution. Changes in potentiodynamic polarization curves are observed not only at different scan rates and electrolytes but also between replicated experiments. Contrary to what was reported in previous studies, the disturbance of charging current associated with high scan rates does not satisfactorily explain the potentiodynamic polarization shape. Instead, the high field model that incorporates the kinetics of anodic oxide growth successfully captures the features of experimental potentiodynamic polarization curves. Compared to Tafel's theory, the high field model explains remarkably the changing kinetics with scan rates, electrolytes, and the variance between measurements performed at different sites.

npj Materials Degradation (2022)6:20; https://doi.org/10.1038/s41529-022-00227-3

INTRODUCTION

Fueled by the need for energy efficiency and the reduction of greenhouse gas emissions, there is an important push of the automotive industry towards lightweighting[1–3]. In this regard, aluminum alloys (AA) have become the materials of choice to compete with traditional steel applications[1,4]. However, within an AA, the presence of more noble alloying elements, responsible for increasing strength, creates micro-galvanic coupling. As a result, these phases lead to localized corrosion and, in some cases, subsequent mechanical failure due to stress corrosion cracking[5,6].

Corrosion is often investigated electrochemically by potentiodynamic polarization (PDP) experiments, both at the macro[7–10] and micro[11–15] scales. However, the corrosion metrics extracted from PDP using the Tafel kinetics laws are sensitive to the fitting procedure and experimental parameters[16–18]. Notably, it is recommended to measure the anodic and cathodic branches separately, starting from the corrosion potential (E_{corr}), and to use a low scan rate of 0.167 mV·s^{-1} [19]. However, under these conditions, the measurements are affected by irreversible surface changes and the accumulation of corrosion products[20]. As such, there is no consensus for the choice of optimal PDP parameters, which leads to inconsistency in interpreting the corrosion kinetics from PDP experiments. Moreover, the degradation of AA by localized corrosion is misinterpreted by macroscale PDP since the damage is concentrated near microstructural features. Therefore, localized corrosion must be investigated at the scale of these microstructural features to accurately assess the long-term durability of AA, which is a critical need in the industry. Since hundreds to thousands of measurements are needed to map a sample's electrochemical properties using microscale techniques, microscale PDP is typically performed at a high scan rate (>10 mV·s^{-1}) in a single scan direction[11,21–23]. Under these conditions, the system is away from its steady-state, and the extracted Tafel parameters will not accurately reflect the corrosion kinetics[20,24]. Hence, at the microscale, PDP is currently relegated as a qualitative corrosion measurement.

Despite the convenience of measuring PDP at a higher scan rate, the effect of scan rates has been seldom studied, and, in these few studies, the scan rates were limited to a narrow range of 0.1 mV·s^{-1} to 10 mV·s^{-1}. The changes appearing at higher scan rates were mostly attributed to double-layer capacitance[20,25,26] and mass transport[24,27]. However, the metals' active dissolution and passivation kinetics under high scan rate PDP has received little attention. This is surprising considering the extensive work on the kinetics of oxide growth on metals[28–36]. Notable work includes the study of aluminum passivation using the high field model by H.S. White[29] and H.S. Isaac[31], and the development of the point defect model by D.D. Mcdonald[37]. Both models show an inherent dependence with scan rates that could account for the changes appearing in PDP at higher scan rates.

Herein, the PDP obtained from AA7075 (nominal composition in Supplementary Table 1) in 0.62 M NaH_2PO_4 and 3.5 wt% NaCl solutions at scan rates up to 100 mV·s^{-1} were analyzed by numerical simulations, taking into account effects of double-layer capacitance as well as the high field model. For both electrolytes, the passivation kinetics described by the high field model played the largest role in predicting the trends observed when varying scan rates.

RESULTS AND DISCUSSION

Complex trends emerge from PDP at high scan rates

The experimental PDP curves of AA7075 in 0.62 M NaH_2PO_4 and 3.5 wt% NaCl are presented in Fig. 1. Prior to the PDP measurement, the sample was at OCP until steady-state is reached: ~20 min for OCP to stabilize at −0.82 V vs. SCE in 0.62 M NaH_2PO_4 and ~5 min for OCP to stabilize at −0.78 V vs. SCE in 3.5 wt% NaCl. Before starting the potential scan in the positive direction, a potential of −0.25 V vs. OCP was then applied for 20 s

[1]Laboratory for Electrochemical Reactive Imaging and Detection of Biological Systems, McGill University, Montreal, QC H3A 0B8, Canada. [2]Automotive and Surface Transportation Research Centre, Division of Transportation and Manufacturing, National Research Council Canada, Aluminum Technology Center, Saguenay, QC G7H 8C3, Canada. [3]These authors contributed equally: Hu Zhou, Danny Chhin. ✉email: alban.morel@cnrc-nrc.gc.ca; danick.gallant@cnrc-nrc.gc.ca; janine.mauzeroll@mcgill.ca

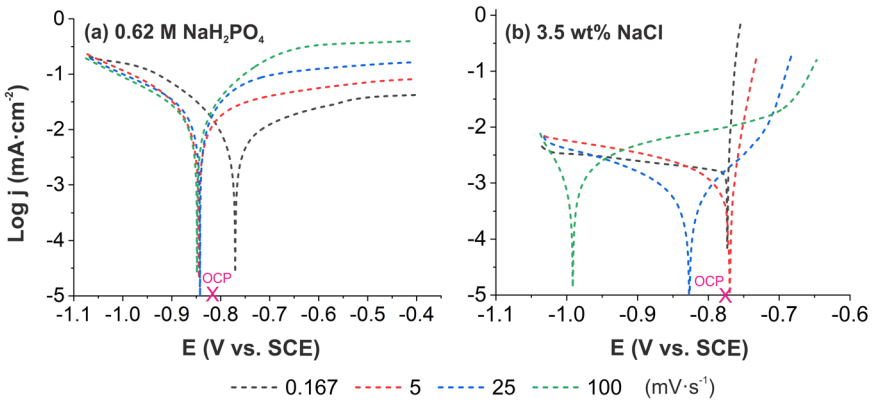

Fig. 1 Experimental PDP of AA7075 at scan rates of 0.167, 5, 25, 100 mV·s^{-1}. PDP measured in (**a**) 0.62 M NaH_2PO_4 and (**b**) 3.5 wt% NaCl solution. The data with a 95% confidence interval is presented in the SI (Supplementary Fig. 1).

to reduce the transient effects such as charging current and diffusion of O_2.

In 0.62 M NaH_2PO_4, the E_{corr} and corrosion current density (j_{corr}) measured at 0.167 mV·s^{-1} (black line in Fig. 1a) are −0.77 V vs. SCE and 9.8 μA·cm^{-2}, respectively, which is in agreement with values from the literature[38]. Under acidic conditions (pH of 3.6), HER is the dominant cathodic reaction[39,40]. At the anodic branch, the current steadily increases until it reaches a current plateau, the critical passivation current, where corrosion proceeds uniformly. At scan rates of 5, 25, and 100 mV·s^{-1} (red, blue, and green lines in Fig. 1a), the E_{corr}^{app} all shift to a similar potential value, ~ −0.848 V vs. SCE comparatively to −0.77 V vs. SCE at 0.167 mV·s^{-1}. Moreover, the anodic branch current magnitude increases with increasing scan rates. The differences from the high scan rates PDP translate into different values of E_{corr} and j_{corr} for each scan rate (Supplementary Table 2). Thus, the 'apparent' superscript is used here to distinguish between the E_{corr} and j_{corr} obtained at 0.167 mV·s^{-1} from the ones obtained at higher scan rate.

In 3.5 wt% NaCl, at pH 7, the E_{corr} and j_{corr} measured at 0.167 mV·s^{-1} (black line in Fig. 1b) are −0.78 V vs. SCE and 1.60 μA·cm^{-2}, respectively, which is in agreement with values from the literature[41–43]. Both the value of j_{corr} and the magnitude of all currents before the onset of pitting are smaller in NaCl compared with those measured in acidic NaH_2PO_4. This observation can be attributed to a less reactive environment for the cathodic reaction and a slower oxide dissolution rate in the neutral solution. The anodic branch does not present the typical passive region since localized pitting corrosion occurs in the presence of aggressive Cl^- ions and pitting initiates at a potential (E_{pit}) very close to E_{corr}[44]. As the scan rate increases (red, blue, and green lines in Fig. 1b), distinct and severe distortions are observed on each PDP curve. Larger shifts of the E_{corr}^{app} are observed for all scan rates in NaCl compared to NaH_2PO_4. The E_{corr}^{app} shift is accompanied by a change in the cathodic branch shape: at 0.167 mV·s^{-1} (black line in Fig. 1b), the cathodic branch appears relatively flat, while at higher scan rates (red, blue, and green lines in Fig. 1b), its slope increases. Moreover, the potential at which stable pitting takes place becomes more positive with the increase in scan rate.

At higher scan rates, a qualitative evaluation of the corrosion process can be drawn from the shifts of the corrosion potential and pitting potential, but due to the drastic distortions observed in the Tafel plots, the extracted apparent Tafel parameters cannot be used quantitatively (Supplementary Table 2). For a specific electrolyte solution, the intrinsic corrosion metrics should not change with scan rates, meaning that the Tafel fit is also capturing processes that accompany a change in scan rate.

The Inability of Capacitive Current to Describe High Scan Rates PDP

The PDP current density (j_{pdp}) can be expressed as a convolution of the current originating from faradaic and capacitive processes.

$$j_{pdp} = j_f + j_{cap} \quad (1)$$

Where j_{pdp} is the PDP current density, j_f is the faradaic current density and j_{cap} is the capacitive current density.

Based on Eq. (2), j_{cap} increases with the scan rate and could potentially explain the PDP trends observed at higher scan rates in Fig. 1[25,45].

$$j_{cap} = C(t)\frac{\partial V}{\partial t} \quad (2)$$

Where C(t) is the capacitance and $\frac{\partial V}{\partial t}$ is the potential scan rate.

In order to evaluate the effect of j_{cap} on high scan rates PDP, the PDP curves at scan rates of 5, 25, and 100 mV·s^{-1} were simulated by calculating j_{pdp} using Eq. (1). The measured PDP current at 0.167 mV·s^{-1} was used as an approximation for j_f (condition where $j_{cap} \rightarrow 0$), while j_{cap} was calculated from Eq. (2). However, determining C(t) is not an easy task as evidenced by the large discrepancy in reported values for AA7075[46–50] which can range from 10 to 3500 μF·cm^{-2}. The inconsistency in measured C(t) for an oxide-covered metal can be attributed in part to interference from corrosion occurring at the metal/oxide/electrolyte interface. C(t) is most often measured by EIS where the chosen equivalent circuit has a major impact in evaluating C(t), but the choice of the equivalent circuit and its physical interpretation remain a contentious subject among corrosion specialists[48,49,51]. Moreover, corrosion of the metal matrix can lead to changes in real surface area due to the etching of the oxide into a porous structure[52–54], causing the value of C(t) to change during the measurements.

Since we are solely interested in evaluating C(t) for AA7075 and not the corrosion kinetics, the EIS measurements were restricted to the higher frequency region (10^5 to 1 Hz) where the capacitive process dominates. The oxide/electrolyte interface is modeled using a solution resistance (R_s) for the electrolyte and a constant phase element (CPE) in parallel with a polarization resistance (R_p) to represent the non-ideal capacitive behavior of the oxide film (Fig. 2a). Here, the CPE is defined as a combination of the electrochemical double layer (C_{dl}) and oxide (C_{ox}) in series, where the total capacitance is often defined by Eq. (3).

$$\frac{1}{C(t)} = \frac{1}{C_{dl}} + \frac{1}{C_{ox}} \quad (3)$$

According to Gharbi et al.[55], Eq. (3) is not accurate for CPE and is only valid at very high frequency or scan rate, where C(t) would be dominated by C_{ox}. At frequency, within the range of typical PDP (1 mV·s^{-1} to 100 mV·s^{-1}) the measured C(t) would be more

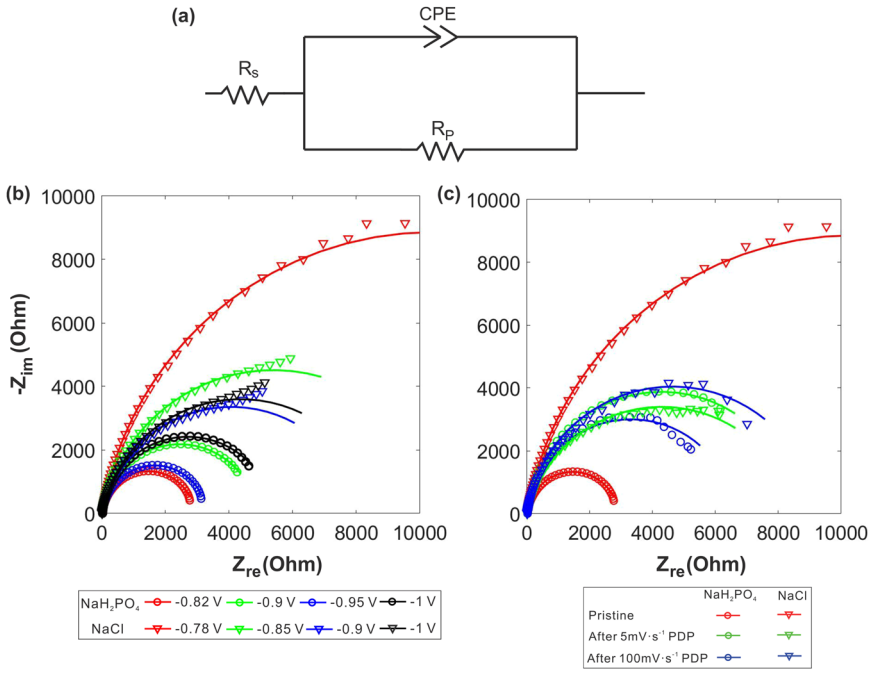

Fig. 2 EIS spectra of AA7075 in 0.62 M NaH_2PO_4 and 3.5 wt% NaCl solution. The frequency range of all measurements is from 10^5 Hz to 1 Hz. **a** The equivalent circuit used to fit the data. **b** Nyquist plot as a function of the applied potential. **c** Nyquist plot as a function of surface conditioning.

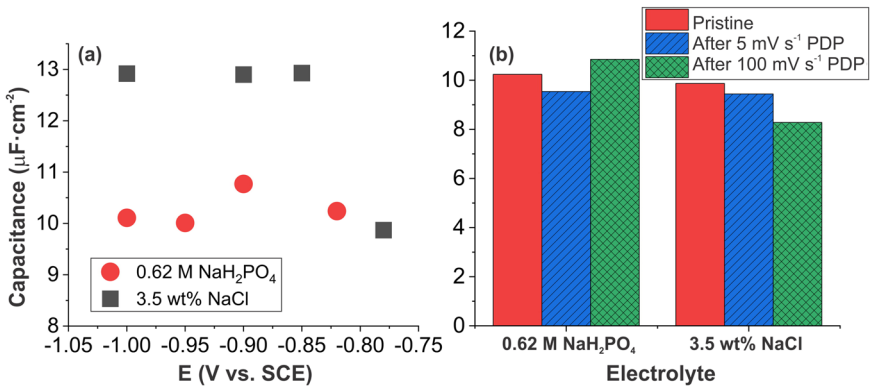

Fig. 3 The capacitance of AA7075 measured by electrochemical impedance spectroscopy (EIS). The capacitance of AA7075 extracted by the Brug equation as a function of (**a**) applied potential and (**b**) sample conditioning (measurements performed at OCP). The error bars represent a 95% confidence interval. Each measurement was done on a fresh spot.

reflective of C_{dl}. This would explain the frequency dependence observed for C(t) on pure aluminum, where they measured a change in C(t) from 35 μF·cm^{-2} at scan rate of 1 mV·s^{-1} to 15 μF·cm^{-2} at scan rate of 2000 mV·s^{-1}. Thus, C(t) was extracted using the Brug equation (Eq. (4)), since it is suited to describe processes with a surface time-constants distribution[56,57].

$$C = Q^{1/\alpha}\left(\frac{R_p R_s}{R_p + R_s}\right)^{1-\alpha/\alpha} \quad (4)$$

Where α and Q are CPE parameters, R_p is the polarization resistance and R_s is the solution resistance. Also, to account for any change in C(t) during the measurement of PDP, EIS measurements were performed at multiple potentials and after conditioning of the sample by PDP at 5 mV·s^{-1} and 100 mV·s^{-1} (Fig. 2b, c). The α for all spectra were above 0.85 (Supplementary Tables 3, 4) and based on Fig. 3, the extracted C(t) is different between both electrolytes but does not vary significantly as a function of the applied potential or the sample conditioning.

The addition of j_{cap} can partially explain some of the changes observed in high scan rates PDPs (Fig. 4) such as the shift of the E_{corr}^{app}, but it does not correctly predict the overall shape of the curves for any scan rates and electrolytes. For example, in 0.62 M NaH_2PO_4 with a C(t) of 300 μF·cm^{-2} (blue line in Fig. 4a), the addition of capacitive current predicts correctly the E_{corr}^{app} shift for the PDP performed at a 100 mV·s^{-1}. However, it fails to do so for slower scan rates, even when accounting for increasing C(t) at slower scan rates. It also fails to fit the anodic branch and to explain any other observed trend, like the overlap of both the cathodic branches and E_{corr}^{app} observed for scan rates of 5, 25, and 100 mV·s^{-1} (Fig. 1a).

A gap, similar to that seen for the anodic branches, would be expected based on the j_{cap} calculated from Eq. (2) with a constant C(t). Similarly, attempts to fit the PDP curves obtained in 3.5 wt% NaCl are unsuccessful (Fig. 4b), even if we disregard the pitting occurring after E_{corr} that is not directly related to the capacitive current. Here C(t) would need to vary drastically, up to 1 or 2

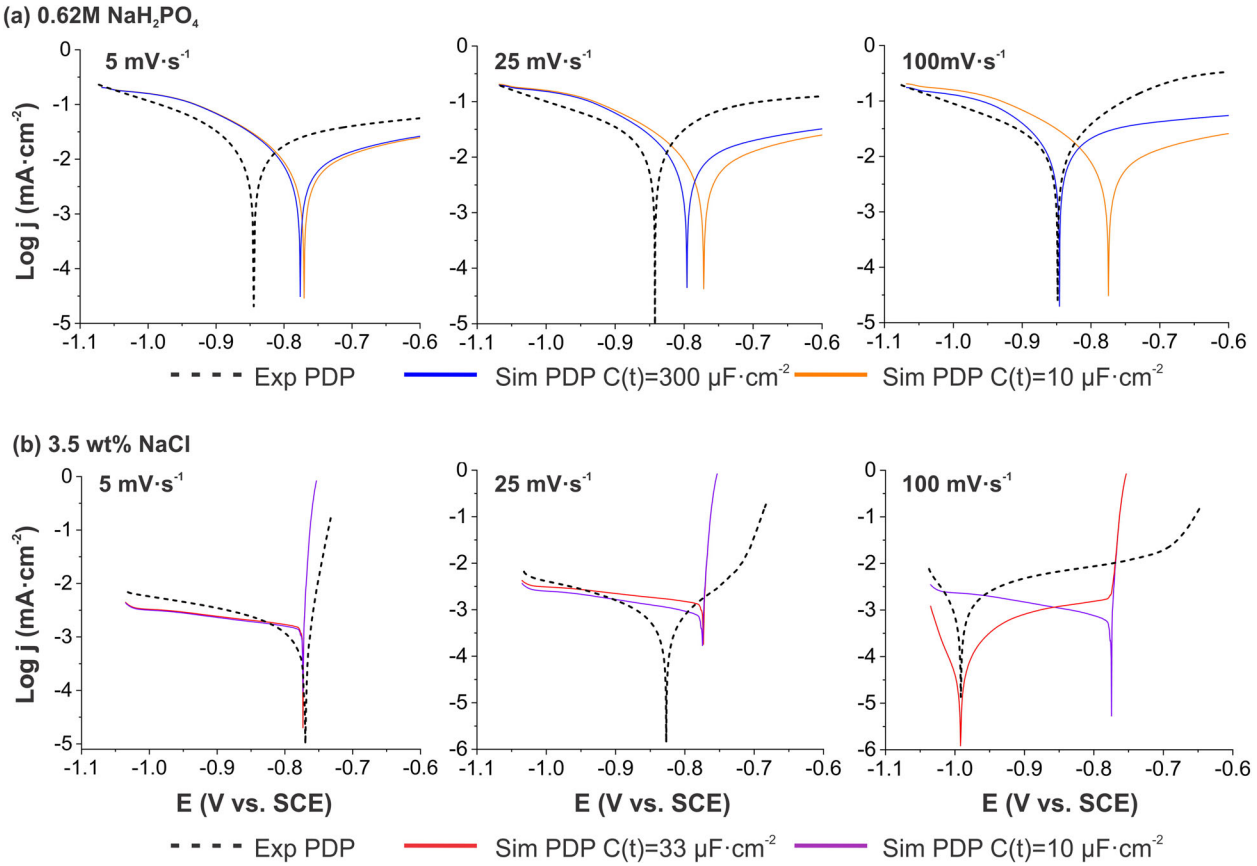

Fig. 4 PDP simulation with addition of capacitive current. Simulated PDP with the addition of a constant capacitive current, j_{cap}. In (**a**) 0.62 M NaH_2PO_4 and (**b**) 3.5 wt% NaCl.

orders of magnitude, as a function of the electrolyte, the potential, and the scan rates, to account for all the observed trends in PDPs at high scan rates. However, such an extensive increase in C(t) is not supported by our EIS measurements (Fig. 3). Thus, the capacitive current alone cannot explain the complex trends observed at different scan rates in both electrolytes, which is surprising since it has often been alluded to be the main contributor to PDP distortion[20,25].

Defining Scan Rate Dependent Processes for Modeling High Scan Rates PDP

Since the addition of capacitive current failed to predict the trends observed in PDP at higher scan rates, we now investigate the current originating from the growth of the oxide layer as described by the high field model. For reactive materials like aluminum alloys, classified as 'valve metals', the corrosion process is inhibited by the spontaneous formation of an insulating oxide film in ambient conditions[32,58]. Radiotracer and secondary ion mass spectrometry[59–62] experiments confirmed that the oxide layer grows at the metal/oxide interface by the migration of OH^-/O^{2-} species (Fig. 5a), and at the oxide/electrolyte interface by the migration of Al^{3+} (Fig. 5b). Equations (5) to (7) summarize the passivation process under such conditions. However, direct dissolution of Al can still occur via field-assisted ejection of Al^{3+} species in solution[63,64] (Fig. 5c).

$$Al \rightarrow Al^{3+} + 3e^- \tag{5}$$

$$H_2O \rightarrow 2H^+ + O^{2-} \tag{6}$$

$$2Al^{3+} + 3H_2O \rightarrow Al_2O_3 + 6H^+ \tag{7}$$

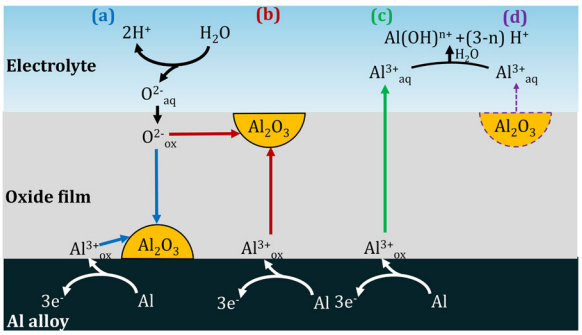

Fig. 5 Concurrent processes considered in the high field model. a Oxide growth at the Al/Oxide interface from the migration of O^{2-}. **b** Oxide growth at the Oxide/Electrolyte interface from the migration of Al^{3+}. **c** Direct ejection and hydrolysis of Al^{3+}. **d** Dissolution of Al_2O_3.

In the high field model, the migration of ionic species across the oxide film is considered the rate-limiting step for the metal oxidation rather than charge transfer. Mott and Cabrera derived the current expression, by defining the potential drop within the oxide film as the main driving force for the migration of ions[65].

$$j_{hf} = A\exp[\beta_a E] \tag{8}$$

$$\mathbf{E} = \frac{\eta}{d} \tag{9}$$

$$\eta = E_{app} - E_{Al_2O_3} \tag{10}$$

Where j_{hf} is the anodic current density derived under the high field model, A and β_a are kinetic parameters that describe the mobility of ions in the oxide, **E** is the magnitude of the electric field, d is the oxide film thickness, η is the overpotential, E_{app} is the applied potential, and $E_{Al_2O_3}$ is the equilibrium potential for the formation of Al_2O_3 described by Eq. (7).

The j_{hf} can be converted into an oxide film growth rate from Faraday's electrolysis law. A passivation efficiency factor (ε_p) was introduced by Lee et al.[64] to differentiate between the j_{hf} fraction that contributes to oxide growth and direct dissolution of Al.

$$\frac{\partial d}{\partial t} = \varepsilon_p j_{hf} \frac{M}{nF\rho} \tag{11}$$

where ε_p is the passivation efficiency (1 = 100% passivation efficiency), M is the molar mass of Al_2O_3, ρ is the density of Al_2O_3, n is the number of electrons transferred, and F is the Faraday's constant.

The oxide film growth is also balanced by the chemical dissolution of Al_2O_3 in solution[29,33] (Fig. 5d), where the dissolution rate is known to be enhanced in acidic/alkaline condition[64,66,67].

$$\frac{\partial d}{\partial t} = -\frac{M}{\rho} R_{diss} \tag{12}$$

Where R_{diss} is the dissolution rate of Al_2O_3.

To determine the electric field magnitude, which depends on the overpotential and the oxide film thickness (Eq. (9)), the change in oxide film thickness during polarization is calculated by integrating the rate of film growth (Eq. (11)), and film dissolution (Eq. (12)).

$$d = d_0 + \varepsilon_p \frac{M}{nF\rho} \int j_{hf}(t)dt - \frac{M}{\rho} \int R_{diss}(t)dt \tag{13}$$

Where d_0 is the thickness of the air-formed oxide film already present at the surface before immersion in the electrolyte. Finally, the anodic current contribution, j_{hf}, can be calculated by solving Eqs. (8) and (13) together.

Table 1. Parameters used in the simulation of j_{hf} in 0.62 M NaH_2PO_4 and 3.5%wt NaCl.

Parameters	NaH_2PO_4	NaCl
C(t) ($\mu F \cdot cm^{-2}$)	16	21
E_c (V vs. SCE)	−0.82	−0.773
$E_{Al_2O_3}$ (V vs. SCE)[70]	−1.9	−2.0
A ($A \cdot cm^{-2}$)[28]	6.5×10^{-12}	6.5×10^{-12}
β_a ($cm \cdot V^{-1}$)[28]	3.6×10^{-6}	3.6×10^{-6}
M ($g \cdot mol^{-1}$)	101.96	101.96
ρ ($g \cdot cm^{-3}$)[28]	3	3
n[28]	6	6

The cathodic current density (j_c) for an AA in an aerated aqueous solution originates from both the hydrogen evolution reaction (HER) and the oxygen reduction reaction (ORR)[62,68].

$$2H^+ + 2e^- \rightarrow H_2 \tag{14}$$

$$O_2 + 2H_2O + 4e^- \rightarrow 4OH^- \tag{15}$$

To make things simpler as we are focusing on the anodic current described by the high field model, we assume that both cathodic reactions can be described by a single Tafel-like expression and that it is not strongly affected by the change in oxide thickness.

$$j_c = -j_c^0 10^{(E_{app} - E_c)/\beta_c} \tag{16}$$

Where j_c is the cathodic current density, j_c^0 is the cathodic exchange current density, E_c is the mixed equilibrium potential for the cathodic reactions, β_c is the cathodic Tafel slope.

So now, the PDP current density, j_{pdp}, can be expressed as the sum of the anodic high field current density, the cathodic current density, and the capacitive current density.

$$j_{pdp} = j_{hf} + j_c + j_{cap} \tag{17}$$

PDP curves were simulated in COMSOL Multiphysics v6.2 using the DAE and ODE physics in 0D to calculate j_{pdp} from Eq. (17), j_{hf} from Eqs. (8) and (13), j_c from Eq. (16) and j_{cap} from Eq. (2) (details are in section 8 of the SI and the COMSOL report is also available). To limit the number of fitting variables, the passivation kinetic parameters A, β_a, discussed in more details in the following sections, were taken from reference[28], by approximating that they do not change significantly between different Al alloys and from an electrolyte to another. The density of Al_2O_3 (ρ) was taken from the literature, however, it can change according to the electrolyte composition and anodization conditions since it will affect the morphology and composition of the oxide film[59,60,69]. The number of electrons, n, involved in the growth of Al_2O_3 is assumed to be 6, based on Eqs. (5) and (7). E_c was approximated by the respective value of OCP in 0.62 M NaH_2PO_4 and 3.5 wt% NaCl, while values of $E_{Al_2O_3}$ were taken from the Pourbaix diagram factoring in the electrolyte pH[70]. Based on our EIS measurements, C(t) of 16 $\mu F \cdot cm^{-2}$ was used for 0.62 M NaH_2PO_4 and 21 $\mu F \cdot cm^{-2}$ for 3.5 wt% NaCl. Although, there is an increase in C(t) as the scan rate decreases, the effect on j_{cap} is negligible within the range of scan rates used in this work (Fig. 4), and C(t) was assumed constant. The parameters taken from the literature are estimates that might not strictly apply in the context of an alloy, but nevertheless, the objective is to demonstrate that the high field model used in this work can explain the experimental PDP trends. All parameters used for the simulations are presented in Table 1. The remaining parameters, most of them hard to characterize accurately, were left to be fitted (R_{diss}, d_0, ε_p, j_c^0, β_c), and a single set of parameters was used to fit measurements from all the scan rates simultaneously (Table 2).

Table 2. Variables obtained by fitting simulation of j_{hf} to experimental PDP in 0.62 M NaH_2PO_4 and 3.5 wt% NaCl.

Fitted variables	NaH_2PO_4 Fitted	NaH_2PO_4 Experimental	NaCl Fitted[a]	NaCl Experimental
d_0 (nm)	2.44	2.38 ± 0.51	2.7	2.38 ± 0.51
R_{diss}[b] ($mol \cdot cm^{-2} \cdot s^{-1}$)(μm per year)	2.1×10^{-11} 225	5.51×10^{-12} 59.1	2.0×10^{-12} 21.5	3.44×10^{-12} 36.9
ε_p	0.85	–	36	–
j_c^0 ($\mu A \cdot cm^{-2}$)	30	–	3.7	–
β_c ($mV \cdot dec^{-1}$)	−250	–	−600	–

[a]To simulate pitting in NaCl, the fitted R_{diss} and ε_p take values of 1×10^{-9} $mol \cdot cm^{-2} \cdot s^{-1}$ and 0, respectively when $E_{app} > -0.773$ V vs. SCE. [b]R_{diss} is given in $mol \cdot cm^{-2} \cdot s^{-1}$ and μm per year.

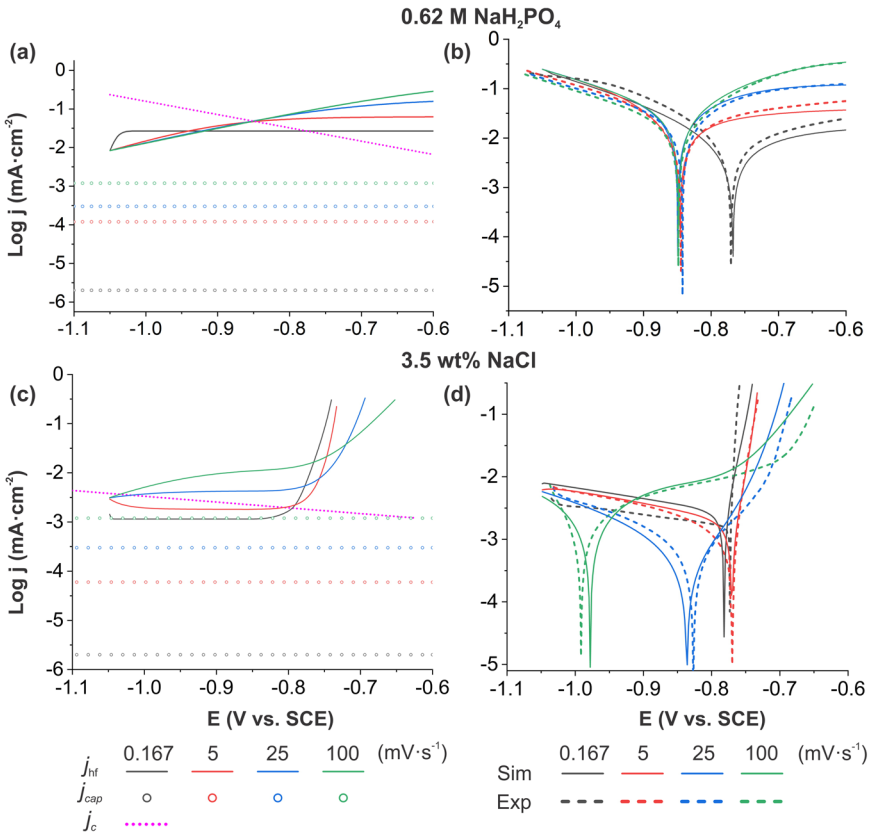

Fig. 6 Simulated PDP with the addition of the high field anodic current, j_{hf}. **a** Simulated j_{hf}, j_{cap}, and j_c for PDP in 0.62 M NaH_2PO_4. **b** Fitted curves for PDP in 0.62 M NaH_2PO_4. **c** Simulated j_{hf}, j_{cap}, and j_c for PDP in 3.5 wt% NaCl. **d** Fitted curves for PDP in 3.5 wt% NaCl.

The Anodic High Field Current as the Dominant Factor in High Scan Rates PDP

The simulated j_{hf} inherently changes with increasing scan rates (Fig. 6a, c). At the beginning of the potential scan, j_{hf} increases exponentially but the progressive thickening of the oxide film (Supplementary Fig. 2) will affect the magnitude of the electric field, **E** (Eq. (9)). Eventually, **E** and the oxide growth rate (Eq. (13)), which is controlled by j_{hf} and R_{diss}, will settle into a dynamic equilibrium, and j_{hf} will converge to a steady-state (j_{ss}). At higher scan rates, a higher potential is reached for the same oxide thickness relative to a slower scan rate (Supplementary Fig. 2a, b), resulting in a larger **E** and j_{hf}. The perception of j_{hf} is further skewed because it is plotted as a function of the potential; for a potential window of 250 mV, the oxide growth is compressed over a 2.5 s interval for a scan rate of 100 mV·s^{-1} but it is stretched over 1497 sec at 0.167 mV·s^{-1}. The end result, as particularly observed in Fig. 6a, is j_{hf} convergence to a steady-state at a less negative potential and a higher current density with increasing scan rates. An analytical expression of the steady-state current (j_{ss}) as a function of the scan rate can be derived from Eq. (8) and Eq. (13) under the assumption of 100% faradaic efficiency and no chemical dissolution[34–36].

$$\ln(j_{ss}) = \ln(A) + \frac{nF\rho\beta_a}{M}\left[\frac{v}{j_{ss}}\right] \tag{18}$$

Where j_{ss} is the steady-state current and v is the scan rate. Thus, the kinetic parameter A and β_a can be determined from the slope and intercept of the $\ln(j_{ss})$ vs. v/j_{ss} plot.

For the reverse case, where the potential is scanned in the negative direction, j_{cap} becomes negative and the **E** decreases from the combined effect of the negative potential scan and oxide growth. For example, in 0.62 M NaH_2PO_4, the large **E** drives a high current, which is followed by the rapid decay of the anodic current due to the oxide growth and negative potential scan (Supplementary Fig. 3). The simulated PDP curves (Supplementary Fig. 3) show that the high field model can describe the trend for the decay of the anodic current for different scan rates.

In the 0.62 M NaH_2PO_4 electrolyte, the E_{corr} visually corresponds to the potential at which j_{hf} and j_c intersect (Fig. 6a) since the contribution from j_{cap} is negligible. At scan rates of 5, 25, and 100 mV·s^{-1}, j_{hf} still increase beyond the steady-state at 0.167 mV·s^{-1}, but they start to diverge as the j_{hf} of higher scan rates continue to increase, while for lower scan rates they settle into a steady-state. However, j_c intersect with j_{hf} from scan rates of 5, 25, and 100 mV·s^{-1} before the j_{hf} are diverging significantly, thus explaining the E_{corr}^{app} overlap and the shift from −0.770 V to −0.848 V vs. SCE (purple dotted line and red, green, blue line in Fig. 6a). Moreover, as can be seen in Fig. 6b, the overall shape and trend of the experimental anodic branches with increasing scan rates match with the simulated j_{hf}. However, the high field model predicts that a steady-state current, j_{ss}, will eventually be reached during the potential scan, but in the experimental anodic branch, the current density keeps increasing, a trend that becomes more apparent as the scan rate is lowered. Lee et al.[64] attributed the continuous increase in j_{ss} to a decrease in passivation efficiency, ε_p, from a change in the surface pH. In an unbuffered solution, the surface pH would drop, thus hindering the formation of O^{2-} produced by water dissociation (Eq. (4)) at the oxide/electrolyte interface, and reducing the probability for Al^{3+} to bond with O^{2-} [64,71]. In our case, the use of an equimolar buffer solution of 0.564 M NaH_2PO_4/0.056 M Na_2HPO_4 (Fig. 7) stabilized j_{ss} by preventing a change in surface pH during the potential scan. Moreover, the difference in pH from 3.6 to 5.5, between both electrolytes, contributed to shifting the onset of oxide growth to a more positive potential and decreasing j_{pdp}. This result highlights the impact of surface pH change on the measured PDP, which can be linked to change in properties such as ε_p, R_{diss}, $E_{Al_2O_3}$, A

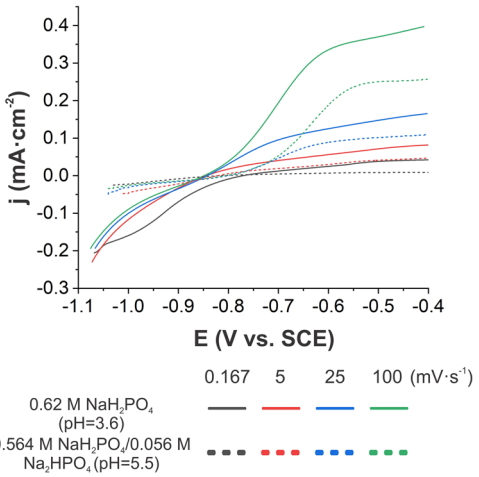

Fig. 7 Effect of pH and buffer on PDP. Current density of PDP measured in 0.62 M NaH_2PO_4 and 0.564 M Na_2HPO_4/0.056 M NaH_2PO_4.

and β_a. Nevertheless, even with the use of constant properties, the inclusion of the j_{hf} parameter in this work can still effectively predict the main changes occurring in a PDP curve at a higher scan rate in the acidic NaH_2PO_4 solution; namely, the shift and the overlap of the cathodic branches and E_{corr}, but also the increase of the anodic branch current density at different scan rates.

In the case of PDP in 3.5 wt% NaCl (Fig. 6c), a step function was used to increase R_{diss} and decrease ε_p, in order to simulate the sudden increase in j_{hf} associated with the occurrence of pitting corrosion. At 0.167 mV·s^{-1}, the measured E_{corr} corresponds to the intersection of j_c with the pitting region of the j_{hf} (purple dotted line and black line in Fig. 6c). While, at higher scan rates 5, 25, and 100 mV·s^{-1}, E_{corr}^{app} is the result of j_c being canceled out by the combined contribution of j_{cap} and j_{hf} transient (purple dotted line and red, green, and blue line in Fig. 6c). Before the occurrence of pitting, the inclusion of j_{hf} captures well the movement of E_{corr}^{app} and the PDP shape across all scan rates (Fig. 6d) from a single set of fitting variables. However, the region near the pitting area is not as well described, indicating that the high field model cannot be used to explain pitting corrosion.

Validation of the high field model parameters

Although the simulated PDP was in good agreement with the experimental data, it relied on a large number of fitting variables and validation is necessary to ensure that the fitted parameters in Table 2 have realistic values. The air-formed oxide thickness was measured by X-ray photoelectron spectroscopy (Supplementary Fig. 4 and Table 4) and an average d_0 value of 2.38 nm with a 95% confidence interval of 0.51 nm was obtained from three measurements in different sites within a 1 cm^2 AA7075 sample. Our values of d_0 used in the simulation for both electrolytes are consistent with our oxide thickness measurement and the ones reported in literature[49,72,73].

The oxide dissolution rate was estimated by quantification of Al ions in their respective electrolyte by ICP-OES after a 24 h exposure. For 3.5 wt% NaCl, the measured dissolution rate agrees with the fitted R_{diss}. For 0.62 M NaH_2PO_4, there is a larger difference between both values, but the difference is still within 1 order of magnitude. Moreover, the measured dissolution is most likely underestimated since it was performed without any polarization of the sample. Under polarization, the sample oxide dissolution rate would be expected to increase as the surface pH change (Fig. 7).

The kinetic parameters A and β_a play a large role in determining the oxide growth rate but it is difficult to characterize them properly. There is a large discrepancy of A and β_a reported in the literature relative to the characterization method used. When it is calculated from the slope and intercept of the linear fit of the ln(j_{ss}) vs. v/j_{ss} plot using Eq. (18), A is on the order of 10^{-6} A·cm^{-2} [34,35], comparatively, it is on the order of 10^{-12} A·cm^{-2} when it is obtained through fitting[30]. In our case it follows the same pattern, the A (4.35×10^{-5} A·cm^{-2}) and β_a (5.17×10^{-7} cm·V^{-1}) calculated from Fig. 8a, are vastly different from the ones used in our simulation ($A = 6.5 \times 10^{-12}$ A·cm^{-2} and $\beta_a = 3.6 \times 10^{-6}$ cm·V^{-1}). When they are used to simulate PDP, it predicts accurately the steady-current, j_{ss}, but vastly overestimates the initial j_{pdp} and gives a poor fit of the PDP. Moreover, the simulated oxide growth (Fig. 8c) is unrealistic in comparison to our initial simulation (Supplementary Fig. 2a), especially at 0.167 mV·s^{-1}. In 0.62 M NaH_2PO_4 and most electrolytes, the passivation efficiency is less than 100%, the oxide dissolves chemically and the high field properties are not constant during a measurement, especially in unbuffered electrolytes (Fig. 7). Thus, the assumption from which Eq. (18) were derived are broken and leads to the erroneous evaluation of A and β_a.

Although Eq. (18) is inaccurate regarding A and β_a, it can still be used to confirm that the oxide growth follows a high field kinetic. Moreover, j_{ss} is accurately calculated by Eq. (18) and can be used to extract j_{ss} at lower scan rates from PDP measurements obtained at high scan rates. This is of particular interest for microscale PDP, where they are typically performed at scan rates upward of 50 mV·s^{-1}. Especially, if the objective is to evaluate the corrosion rate occurring at OCP, it is not necessary to obtain a perfect fit but rather to extrapolate j_{ss} for low scan rate (≤0.167 mV·s^{-1}), where the system is close to steady-state.

Before the occurrence of pitting, R_{diss} and more importantly j_c, are higher in NaH_2PO_4 compared to NaCl (Table 2). This is consistent with results from the literature, where corrosion is found to be more active under acidic or alkaline conditions in a process known as cathodic dissolution[74,75]. The greater dissolution rate of Al_2O_3 in acidic conditions leads to higher cathodic activity and higher repassivation rate, which increases j_c and j_{hf}, respectively[28]. Similarly, in 0.62 M NaH_2PO_4, ε_p is smaller than 1 because in acidic conditions, the production of O^{2-} from the water dissociation reaction, essential to produce Al_2O_3 (see the mechanism in Fig. 5), is unfavorable. But the value of ε_p in 3.5 wt% NaCl is exceptionally high, knowing that it should be bound between 0 and 1. Physically, this high passivation efficiency rendered by the model means that the electric field, E, drops faster than what would normally be predicted by the high field model from an increase in oxide layer thickness (Eqs. (9) and (13)). It is not clear if it is a sign that the high field model does not apply in this case, especially since a ln(j_{ss}) vs. v/j_{ss} plot could not be obtained to confirm the high field growth of the oxide due to the occurrence of pitting before the appearance of a steady-state current. Alternatively, this could be the result of unaccounted processes that are not presently considered in the high field model, especially considering the good prediction obtained using the high field model (Fig. 6d). For example, all properties were assumed to be constant, but this assumption might be incorrect for certain electrolytes or AA. The oxide layer properties are known to change as it grows from the incorporation of ions present in the electrolyte[59], especially for chloride ions[69]. For unbuffered electrolytes, there can be a significant change in pH at the surface of the metal which in turn can affect the dissolution rate and potential for oxide growth, $E_{Al_2O_3}$ (Fig. 7). However, from these results, it is still clear that oxide growth plays a large part in the anodic current density observed.

Correlation Between the Increasing Variance from PDP at Higher Scan Rates and the Oxide Layer Thickness

Another characteristic of PDP obtained at high scan rates is the larger variance between replicates. For example, j_{pdp} in 3.5 wt% at

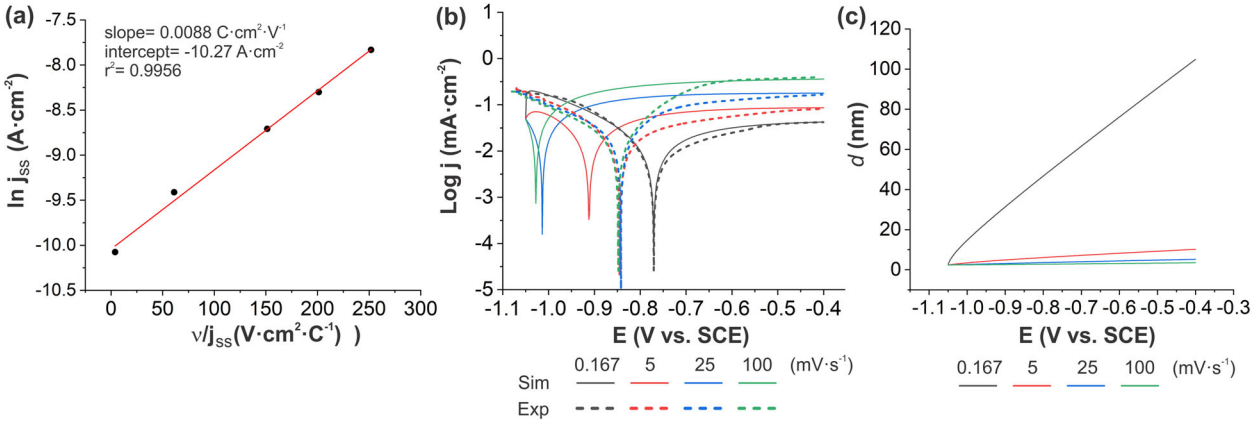

Fig. 8 Validation of A and β_a values reported in literature. a Plot of ln(j_{ss}) vs. ν/j_{ss} based on the values of j_{pdp} at −0.4 V for scan rates of 0.167, 5, 25, 50 and 100 mV·s^{-1} in 0.62 M NaH_2PO_4. **b** Simulated PDP in 0.62 M NaH_2PO_4 with $A = 4.35 \times 10^{-5}$ A·cm^{-2} and $\beta_a = 5.17 \times 10^{-7}$ cm·V^{-1} obtained from (**a**). **c** Simulated d with the same A and β_a in (**b**).

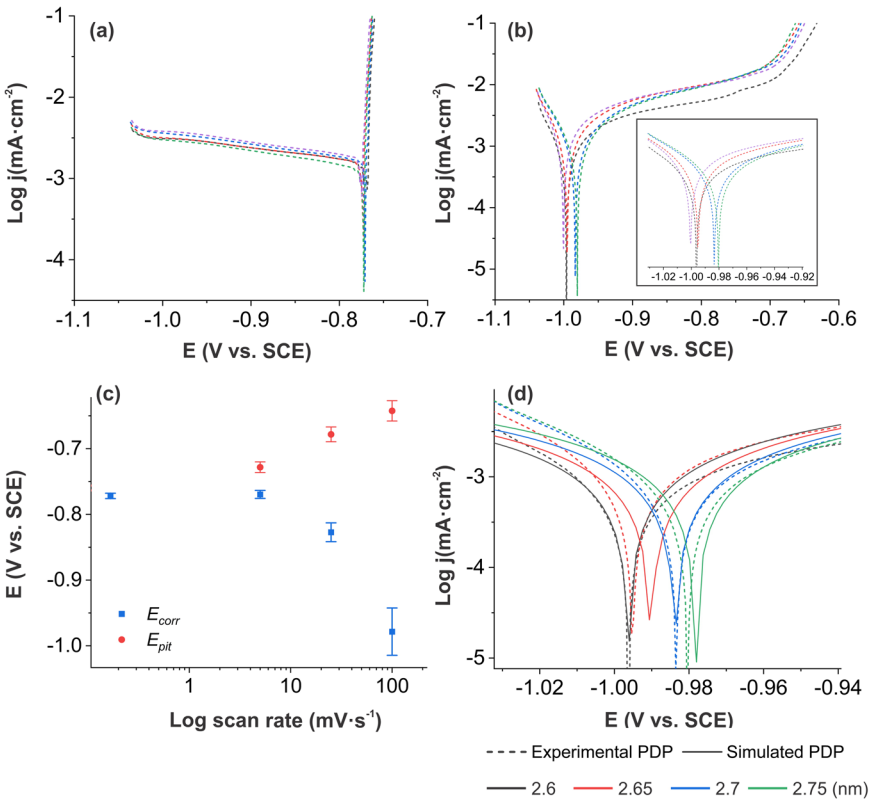

Fig. 9 Effect of scan rates on the variance between PDP replicates in 3.5 wt% NaCl. a 5 PDP replicates at 0.167 mV·s^{-1}. **b** 5 PDP replicates at 100 mV·s^{-1}, the inset shows an enlargement of the E_{corr} region. **c** Distribution of the E_{corr} and E_{pit} at scan rates of 0.167, 5, 25, and 100 mV·s^{-1}. Error bars represent the standard deviation of data of 5 replicates at each scan rate. **d** Simulated effect of air-formed oxide thickness, d_0, and comparison with PDP replicates measured at 100 mV·s^{-1}.

0.167 mV·s^{-1} varies slightly, but overall, the shape of each replicate is virtually the same and they mostly overlap (Fig. 9a). However, at 100 mV·s^{-1}, the difference between each replicate (Fig. 9b) becomes much more apparent and it translates into a much larger distribution of E_{corr}^{app} and E_{pit}, which was determined by the onset of the pitting current from the PDP (Fig. 9c). Consequently, PDP curves obtained at higher scan rates are less reproducible compared to those obtained at slower scan rates. Furthermore, for this work, the increased variance from high scan rates PDP contributes to a larger error in the fitting procedure.

Under the high field model, for the same difference in the value of an AA property, such as the air-formed oxide layer thickness (d_0), the disparity in j_{hf} will be larger for higher scan rates, making it more sensitive to a slight difference in properties. This could explain the increase in variance observed between each replicate PDP performed at higher scan rates since a different region of the sample is probed per replicate. To verify this, PDP curves were simulated with d_0, ranging from 2.60 to 2.75 nm and they were able to emulate the E_{corr}^{app} trend seen in PDP replicates (Fig. 9d). However, it is unclear what the variance in j_{hf} at the macroscale entails since the properties are averaged over a large area.

Investigation at the microscale will be required for a better understanding of the observed variance at high scan rates.

In conclusion, the j_{hf} was the dominant factor over capacitive current in explaining the characteristics of PDP emerging at higher scan rates for AA7075. Compared to the Tafel equations, the high field model can describe, using a single set of parameters, the PDP trends in 2 different electrolytes and for multiple scan rates. Moreover, the kinetics is defined in terms of the oxide layer where some of the parameters (d_0, R_{diss}, ε_p) have a physical meaning that is complementary to the information conventionally obtained from PDP measurements (e.g., j_{corr}, E_{corr}, E_{pit}).

This work is also crucial in bringing microscale PDP measurements, which require these high scan rates, to the rank of quantitative techniques, but important issues need to be addressed beforehand:

- Improve the quality of characterization of the high field model key parameters.
- A better understanding of the effect of localized corrosion events such as micro-galvanic coupling and local oxide breakdown by chloride ions in relation to the high field model.

METHODS

Materials and Sample Preparation

AA7075 samples were provided by the NRC (National Research Council Canada, Saguenay), which were then cut into 8 x 5 cm pieces of 2 mm thickness. Samples were lightly abraded using a general-purpose hand pad (Scotch Brite™). All samples were successively rinsed with anhydrous ethanol (Greenfield Global, Canada) and Milli-Q water (Millipore, 18.2 MΩ·cm resistivity at 25 °C), and then dried under a stream of air. The electrolyte solutions were prepared with NaCl (99.0% purity, Sigma-Aldrich) and NaH_2PO_4 (≥99.0%, Sigma-Aldrich) in Milli-Q water. The solution's pH was measured using a pH meter (XL200, Fisherbrand™) which was calibrated in buffer solutions of pH 4, 7, and 10.

Instrumentation

Electrochemical measurements were performed with a multi-channel VSP-300 potentiostat (Biologic Science Instruments, France) in a Faradaic cage. A three-electrode corrosion cell (K0235 Flat Cell, Princeton Applied Research, AMETEK Scientific Instrument) with an exposed working area of 1 cm^2 was used for all electrochemical measurements, with a saturated calomel electrode (SCE) (CHI 150, CH Instruments) as the reference electrode and a platinum mesh (2.54 cm × 2.54 cm, Goodfellow) as the counter electrode.

Potentiodynamic Polarization Measurements

The experimental procedure was based on standards ASTM G5-94[19] and ASTM G61-86[76]. Naturally aerated 3.5 wt% NaCl and 0.62 M NaH_2PO_4 solutions were used as the electrolyte solutions for all the electrochemical tests to simulate severe corrosion conditions. In both electrolytes, prior to PDP measurements, the sample was left under open circuit potential (OCP) until the variation in OCP fell below 10 mV per minute. Then the sample potential was held at −0.25 V vs. OCP for 20 s before acquiring complete PDP curves at scan rates of 0.167, 5, 25, and 100 mV·s^{-1}, from −0.25 V vs. OCP to 1 V vs. SCE (with a current density cutoff of 1 mA·cm^{-2}). PDP curves were acquired in 5 replicates per scan rate and the average value is considered for analysis. For each measurement, a new uncorroded 1 cm^2 area of the sample was exposed. All the presented current densities (j) are normalized to the geometric area of the working electrode.

Electrochemical Impedance Spectroscopy

Electrochemical impedance spectroscopy (EIS) measurements were performed in potentiostatic mode with a voltage perturbation amplitude of 10 mV (V_{rms} = 7.07 mV) in the frequency range from 10^5 to 1 Hz, in both 0.62 M NaH_2PO_4 and 3.5 wt% NaCl. The measurements were also performed at multiple potentials between −1 V vs. SCE to OCP, as well as before and after PDP measurements. Equivalent circuit fitting was performed using EC-lab (Biologic Science Instruments, France) version 11.33.

X-ray Photoelectron Spectroscopy

XPS analyses were carried out using an Al Kα X-ray photoelectron spectrometer (Thermo Scientific, K-Alpha). The beam size was 400 µm in diameter, the take-off angle of the beam was 90° and ten scans were performed per spectrum. The peak fitting was performed using the Avantage software (Thermo Scientific) using a 'smart' background which is based on the 'Shirley' background with the additional constraint that it should not be of a greater intensity than the actual data at any point in the region. For asymmetric Al 2p (metal) peaks, tail mix and tail exponents were allowed. A spin-orbit splitting ratio of 1:2 was assigned to aluminum metal peaks $2p_{1/2}$ and $2p_{3/2}$.

Inductively Coupled Plasma Optical Emission Spectroscopy

To measure the dissolution rate of Al_2O_3 in 3.5 wt% and 0.62 M NaH_2PO_4, the AA7075 samples were immersed in both electrolytes for 24 h. Then the sample solutions were collected, by rinsing the AA7075 surface with 5% v/v with nitric acid to dissolve any precipitated Al ions for measurements by ICP-OES (Agilent 5100, USA). The wavelengths of Al at 308.215 nm, 394.401 nm, 396.152 nm with minimal elemental interference were chosen as the analytical line. The Al^{3+} standard solutions were prepared in concentrations of 1 ppm, 10 ppm, 20 ppm, and 50 ppm by addition of $AlCl_3$ powder to the electrolyte of interest (NaCl or NaH_2PO_4) which were acidified to a concentration of 5% v/v with nitric acid.

DATA AVAILABILITY

The data sets generated during and/or analyzed during the current study are available from the corresponding author upon reasonable request.

CODE AVAILABILITY

The COMSOL file is available from the corresponding author upon reasonable request.

Received: 9 August 2021; Accepted: 8 February 2022;
Published online: 17 March 2022

REFERENCES

1. Cole, G. & Sherman, A. Light weight materials for automotive applications. *Mater. Charact.* **35**, 3–9 (1995).
2. Fridlyander, I. et al. Aluminum alloys: promising materials in the automotive industry. *Met. Sci. Heat. Treat.* **44**, 365–370 (2002).
3. Abro, S. H., Chandio, A., Channa, I. A. & Alaboodi, A. S. Role of automotive industry in global warming. *Pak. J. Sci. Ind. Res. A: Phys. Sci.* **62**, 197–201 (2019).
4. Dursun, T. & Soutis, C. Recent developments in advanced aircraft aluminium alloys. *Mater. Des.* **56**, 862–871 (2014).
5. Speidel, M. O. Stress corrosion cracking of aluminum alloys. *Metall. Trans. A* **6**, 631 (1975).
6. Sieradzki, K. & Newman, R. Stress-corrosion cracking. *J. Phys. Chem. Solids* **48**, 1101–1113 (1987).
7. Al Saadi, S., Yi, Y., Cho, P., Jang, C. & Beeley, P. Passivity breakdown of 316L stainless steel during potentiodynamic polarization in NaCl solution. *Corros. Sci.* **111**, 720–727 (2016).
8. Yi, Y., Cho, P., Al Zaabi, A., Addad, Y. & Jang, C. Potentiodynamic polarization behaviour of AISI type 316 stainless steel in NaCl solution. *Corros. Sci.* **74**, 92–97 (2013).
9. Liu, X., MacDonald, D. D., Wang, M. & Xu, Y. Effect of dissolved oxygen, temperature, and pH on polarization behavior of carbon steel in simulated concrete pore solution. *Electrochim. Acta* **366**, 137437 (2021).
10. Morshed-Behbahani, K., Zakerin, N., Najafisayar, P. & Pakshir, M. A survey on the passivity of tempered AISI 420 martensitic stainless steel. *Corros. Sci.* **183**, 109340 (2021).
11. Li, Y., Morel, A., Gallant, D. & Mauzeroll, J. Oil-Immersed Scanning Micropipette Contact Method Enabling Long-term Corrosion Mapping. *Anal. Chem.* **92**, 12415–12422 (2020).
12. Shkirskiy, V. et al. Nanoscale Scanning Electrochemical Cell Microscopy and Correlative Surface Structural Analysis to Map Anodic and Cathodic Reactions on Polycrystalline Zn in Acid Media. *J. Electrochem. Soc.* **167**, 041507 (2020).
13. Yule, L. et al. Nanoscale electrochemical visualization of grain-dependent anodic iron dissolution from low carbon steel. *Electrochim. Acta* **332**, 135267 (2020).

14. Yule, L. C., Bentley, C. L., West, G., Shollock, B. A. & Unwin, P. R. Scanning electrochemical cell microscopy: A versatile method for highly localised corrosion related measurements on metal surfaces. *Electrochim. Acta* **298**, 80–88 (2019).
15. Pao, L., Muto, I. & Sugawara, Y. Pitting at inclusions of the equiatomic CoCrFeMnNi alloy and improving corrosion resistance by potentiodynamic polarization in H2SO4. *Corros. Sci.* **191**, 109748 (2021).
16. Revie, R. W. *Corrosion and corrosion control: an introduction to corrosion science and engineering*, 4th edition (John Wiley & Sons, 2008).
17. Poorqasemi, E., Abootalebi, O., Peikari, M. & Haqdar, F. Investigating accuracy of the Tafel extrapolation method in HCl solutions. *Corros. Sci.* **51**, 1043–1054 (2009).
18. Stephens, L. et al. Development of a model for experimental data treatment of diffusion and activation limited polarization curves for magnesium and steel alloys. *J. Electrochem. Soc.* **164**, E3576 (2017).
19. ASTM Standards. G5-94, Standard reference test method for making potentiostatic and potentiodynamic anodic polarization measurements. *Annual book of ASTM Standards, ASTM International*, **3** (2004).
20. Zhang, X., Jiang, Z. H., Yao, Z. P., Song, Y. & Wu, Z. D. Effects of scan rate on the potentiodynamic polarization curve obtained to determine the Tafel slopes and corrosion current density. *Corros. Sci.* **51**, 581–587 (2009).
21. Williams, C. G., Edwards, M. A., Colley, A. L., Macpherson, J. V. & Unwin, P. R. Scanning micropipet contact method for high-resolution imaging of electrode surface redox activity. *Anal. Chem.* **81**, 2486–2495 (2009).
22. Ebejer, N., Schnippering, M., Colburn, A. W., Edwards, M. A. & Unwin, P. R. Localized high resolution electrochemistry and multifunctional imaging: Scanning electrochemical cell microscopy. *Anal. Chem.* **82**, 9141–9145 (2010).
23. Takahashi, Y. et al. Nanoscale visualization of redox activity at lithium-ion battery cathodes. *Nat. Commun.* **5**, 5450 (2014).
24. Fischer, D. A., Vargas, I. T., Pizarro, G. E., Armijo, F. & Walczak, M. The effect of scan rate on the precision of determining corrosion current by Tafel extrapolation: A numerical study on the example of pure Cu in chloride containing medium. *Electrochim. Acta* **313**, 457–467 (2019).
25. ASTM Standard. G102-89, Standard Practice for Calculation of Corrosion Rates and Related Information from Electrochemical Measurements. *Annual Book of ASTM Standards, ASTM International*, **3** (2006).
26. Birbilis, N., Padgett, B. N. & Buchheit, R. G. Limitations in microelectrochemical capillary cell testing and transformation of electrochemical transients for acquisition of microcell impedance data. *Electrochim. Acta* **50**, 3536–3544 (2005).
27. Otieno-Alego, V., Hope, G., Flitt, H. & Schweinsberg, D. The corrosion of a low alloy steel in a steam turbine environment: the effect of oxygen concentration and potential scan rate on input parameters used to computer match the experimental polarization curves. *Corros. Sci.* **37**, 509–525 (1995).
28. Mi, C., Lakhera, N., Kouris, D. A. & Buttry, D. A. Repassivation behaviour of stressed aluminium electrodes in aqueous chloride solutions. *Corros. Sci.* **54**, 10–16 (2012).
29. Boxley, C. J., Watkins, J. J. & White, H. S. Al_2O_3 Film Dissolution in Aqueous Chloride Solutions. *Electrochem. Solid-State Lett.* **6**, B38 (2003).
30. Lee, S. & White, H. S. Dissolution of the native oxide film on polycrystalline and single-crystal aluminum in NaCl solutions. *J. Electrochem. Soc.* **151**, B479 (2004).
31. Lee, H., Xu, F., Jeffcoate, C. S. & Isaacs, H. S. Cyclic Polarization behavior of aluminum oxide films in near neutral solutions. *Electrochem. Solid-State Lett.* **4**, B31 (2001).
32. Linarez Pérez, O. E., Fuertes, V. C. & Pérez, M. A. & López Teijelo, M. Characterization of the anodic growth and dissolution of oxide films on valve metals. *Electrochem. Commun.* **10**, 433–437 (2008).
33. Boxley, C. J. & White, H. S. Relationship Between Al_2O_3 Film Dissolution Rate and the Pitting Potential of Aluminum in NaCl Solution. *J. Electrochem. Soc.* **151**, B265 (2004).
34. Gudić, S., Radošević, J., Krpan-Lisica, D. & Kliškić, M. Anodic film growth on aluminium and Al–Sn alloys in borate buffer solutions. *Electrochim. Acta* **46**, 2515–2526 (2001).
35. Hasenay, D. & Šeruga, M. The growth kinetics and properties of potentiodynamically formed thin oxide films on aluminium in citric acid solutions. *J. Appl. Electrochem.* **37**, 1001–1008 (2007).
36. Williams, D. & Wright, G. Nucleation and growth of anodic oxide films on bismuth —I. Cyclic voltammetry. *Electrochim. Acta* **21**, 1009–1019 (1976).
37. Macdonald, D. D. The point defect model for the passive state. *J. Electrochem. Soc.* **139**, 3434 (1992).
38. Burleigh, T., Rennick, R. & Bovard, F. Corrosion potential for aluminum alloys measured by ASTM G 69. *Corrosion* **49** (1993).
39. Abdel-Gaber, A., Abd-El-Nabey, B., Sidahmed, I., El-Zayady, A. & Saadawy, M. Inhibitive action of some plant extracts on the corrosion of steel in acidic media. *Corros. Sci.* **48**, 2765–2779 (2006).
40. Khaled, K. & Al-Qahtani, M. The inhibitive effect of some tetrazole derivatives towards Al corrosion in acid solution: Chemical, electrochemical and theoretical studies. *Mater. Chem. Phys.* **113**, 150–158 (2009).
41. Osório, W. R., Freitas, E. S. & Garcia, A. EIS and potentiodynamic polarization studies on immiscible monotectic Al–In alloys. *Electrochim. Acta* **102**, 436–445 (2013).
42. Arnott, D., Hinton, B. W. & Ryan, N. Cationic film-forming inhibitors for the corrosion protection of AA 7075 aluminum alloy in chloride solutions. *Mater. Perform.* **26**, 42–47 (1987).
43. Andreatta, F., Terryn, H. & De Wit, J. Corrosion behaviour of different tempers of AA7075 aluminium alloy. *Electrochim. Acta* **49**, 2851–2862 (2004).
44. Nisancioglu, K. & Holtan, H. Measurement of the critical pitting potential of aluminium. *Corros. Sci.* **18**, 835–849 (1978).
45. Newman, J. & Thomas-Alyea, K. E. *Electrochemical systems*, 3rd edition (John Wiley & Sons, 2012).
46. Martin, F., Cheek, G., O'grady, W. & Natishan, P. Impedance studies of the passive film on aluminium. *Corros. Sci.* **47**, 3187–3201 (2005).
47. Orlikowski, J., Ryl, J., Jarzynka, M., Krakowiak, S. & Darowicki, K. Instantaneous impedance monitoring of aluminum alloy 7075 corrosion in borate buffer with admixed chloride ions. *Corrosion* **71**, 828–838 (2015).
48. Visser, P., Terryn, H. & Mol, J. M. Active corrosion protection of various aluminium alloys by lithium-leaching coatings. *Surf. Interface Anal.* **51**, 1276–1287 (2019).
49. Evertsson, J. et al. The thickness of native oxides on aluminum alloys and single crystals. *Appl. Surf. Sci.* **349**, 826–832 (2015).
50. Frers, S., Stefenel, M., Mayer, C. & Chierchie, T. AC-Impedance measurements on aluminium in chloride containing solutions and below the pitting potential. *J. Appl. Electrochem.* **20**, 996–999 (1990).
51. Wang, F., Li, Y., Zhang, Y. & Chen, G. A method to select the optimal equivalent electrical circuit applied to study corrosion system of composite coating on magnesium alloy. *Phys. Lett. A* **384**, 126452 (2020).
52. Kwolek, P. Corrosion behaviour of 7075 aluminium alloy in acidic solution. *RSC Adv.* **10**, 26078–26089 (2020).
53. Torbati-Sarraf, H., Stannard, T. J., La Plante, E. C., Sant, G. N. & Chawla, N. Direct observations of microstructure-resolved corrosion initiation in AA7075-T651 at the nanoscale using vertical scanning interferometry (VSI). *Mater. Charact.* **161**, 110166 (2020).
54. Wu, Z., Richter, C. & Menon, L. A Study of Anodization Process during Pore Formation in Nanoporous Alumina Templates. *J. Electrochem. Soc.* **154**, E8 (2007).
55. Gharbi, O., Tran, M. T., Tribollet, B., Turmine, M. & Vivier, V. Revisiting cyclic voltammetry and electrochemical impedance spectroscopy analysis for capacitance measurements. *Electrochim. Acta* **343**, 136109 (2020).
56. Orazem, M. E. et al. Dielectric properties of materials showing constant-phase-element (CPE) impedance response. *J. Electrochem. Soc.* **160**, C215 (2013).
57. Hirschorn, B. et al. Determination of effective capacitance and film thickness from constant-phase-element parameters. *Electrochim. Acta* **55**, 6218–6227 (2010).
58. Lohrengel, M. Thin anodic oxide layers on aluminium and other valve metals: high field regime. *Mater. Sci. Eng., R.* **11**, 243–294 (1993).
59. Wood, G., Skeldon, P., Thompson, G. & Shimizu, K. A model for the incorporation of electrolyte species into anodic alumina. *J. Electrochem. Soc.* **143**, 74 (1996).
60. Thompson, G. et al. Anodic oxidation of aluminium. *Philos. Mag. B* **55**, 651–667 (1987).
61. Bunker, B. C. et al. Hydration of Passive Oxide Films on Aluminum. *J. Phys. Chem. B* **106**, 4705–4713 (2002).
62. Despić, A. & Parkhutik, V. P. Electrochemistry of Aluminum in Aqueous Solutions and Physics of Its Anodic Oxide, in *Modern aspects of electrochemistry* (Vol. 20, Springer, 1989).
63. Snizhko, L. O. et al. A model for galvanostatic anodising of Al in alkaline solutions. *Electrochim. Acta* **50**, 5458–5464 (2005).
64. Lee, H. & Isaacs, H. S. Growth of Anodic Aluminum Oxide Films Without pH-Buffer. *ECS Trans.* **11**, 121 (2008).
65. Cabrera, N. & Mott, N. F. Theory of the oxidation of metals. *Rep. Prog. Phys.* **12**, 163–184 (1949).
66. Adhikari, S. & Hebert, K. R. Participation of aluminum hydride in the anodic dissolution of aluminum in alkaline solutions. *J. Electrochem. Soc.* **155**, C189 (2008).
67. Nguyen, T. H. & Foley, R. T. The Chemical Nature of Aluminum Corrosion: III . The Dissolution Mechanism of Aluminum Oxide and Aluminum Powder in Various Electrolytes. *J. Electrochem. Soc.* **127**, 2563 (1980).
68. Hughes, A. E., Mol, J. M., Zheludkevich, M. L. & Buchheit, R. G. *Active Protective Coatings: New-Generation Coatings for Metals*, Vol. 233 (Springer, 2016).
69. Natishan, P. & O'grady, W. Chloride ion interactions with oxide-covered aluminum leading to pitting corrosion: a review. *J. Electrochem. Soc.* **161**, C421 (2014).
70. Gimenez, P., Rameau, J. & Reboul, M. Experimental pH potential diagram of aluminum for sea water. *Corrosion* **37**, 673–682 (1981).
71. McCafferty, E. *Surface Chemistry of Aqueous Corrosion Processes*. (Springer, 2015).
72. Strohmeier, B. R. An ESCA method for determining the oxide thickness on aluminum alloys. *Surf. Interface Anal.* **15**, 51–56 (1990).
73. Alexander, M., Thompson, G., Zhou, X., Beamson, G. & Fairley, N. Quantification of oxide film thickness at the surface of aluminium using XPS. *Surf. Interface Anal.* **34**, 485–489 (2002).
74. Thomas, S., Birbilis, N., Venkatraman, M. & Cole, I. Corrosion of zinc as a function of pH. *Corrosion* **68**, 015009-1–015009-9 (2012).

75. Zaid, B., Saidi, D., Benzaid, A. & Hadji, S. Effects of pH and chloride concentration on pitting corrosion of AA6061 aluminum alloy. *Corros. Sci.* **50**, 1841–1847 (2008).
76. ASTM Standard. G61-86, Standard Test Method for Conducting Cyclic Potentiodynamic Polarization Measurements for Localized Corrosion Susceptibility of Iron, Nickel-, or Cobalt-based Alloys. *Annual Book of ASTM Standards, ASTM International*, **3** (2014).

ACKNOWLEDGEMENTS

We acknowledge the financial support from G234176 NSERC RGPIN-2020-04609 and G248536 CQRDA/NRC. This work was conducted as part of a project funded by the NRC's METALTec industrial research group, the Centre québécois de recherche et de développement de l'aluminium (CQRDA), as well as the Canadian Office for Energy Research and Development (OERD). The authors would like to acknowledge Dr. Lihong Shang from McGill Institute for Advanced Materials for her help with the XPS measurements as well as the METALTec industrial research group members and sponsors that supported this investigation and publication.

AUTHOR CONTRIBUTIONS

H.Z. and D.C. are co-first authors. H.Z. performed all experiments. D.C. performed the COMSOL simulation. H.Z and D.C. analyzed the data, discussed the results, and co-wrote the paper. J.M. supervised the project. A.M. and D.G. discussed the results and advised the work. All authors contributed to revision of the manuscript.

COMPETING INTERESTS

The authors declare no competing interests.

ADDITIONAL INFORMATION

Supplementary information The online version contains supplementary material available at https://doi.org/10.1038/s41529-022-00227-3.

Correspondence and requests for materials should be addressed to Alban Morel, Danick Gallant or Janine Mauzeroll.

Reprints and permission information is available at http://www.nature.com/reprints

Publisher's note Springer Nature remains neutral with regard to jurisdictional claims in published maps and institutional affiliations.